2024 IEEE International Conference on Robotics and Automation (ICRA 2024)
May 13-17, 2024. Yokohama, Japan

Non-singular Fast Terminal Adaptive Visual Tracking Control with Reduced Tuning Parameters for an Aerial Vehicle Under Perturbations

Gustavo Olivas-Martínez, Armando Miranda-Moya, Carlos Katt, and Herman Castañeda

Abstract— **This paper presents a robust image-based visual servoing design for a quad-rotor unmanned aerial vehicle performing a visual target-tracking operation in the presence of turbulent wind. Image information is extracted and processed to control the positioning and heading of the aerial vehicle. A novel adaptive non-singular fast terminal sliding mode strategy is introduced to manage the visual servoing error. Unlike other sliding mode methods, the proposed approach diminishes the complexity of the system due to the reduction of its control parameters while providing practical finite-time convergence, robustness against bounded external disturbances and model uncertainties, non-overestimation of the control gains, and chattering attenuation. Furthermore, the stability of the system in closed loop is guaranteed through Lyapunov theory. Finally, simulation results demonstrate the capabilities and performance of such a controller in a high-fidelity scenario using the Robot Operating System and Gazebo frameworks.**

I. Introduction

Image-based visual servoing (IBVS) is a computationally efficient technique where image information is utilized as feedback signals to control the movement of a robot [1]. Unlike traditional non-visual navigation schemes such as global navigation satellite system (GNSS)-based strategies, it offers a higher position accuracy even if uncertainties regarding the camera-robot system calibration are present [2]. Furthermore, IBVS systems estimate the position error between the robot and its target based directly on a set of features from the 2D image [3]. Thus, they are suitable for applications involving GNSS-denied areas [4], micro-manipulation systems [5], obstacle avoidance [6], landing tasks for unmanned aerial vehicles (UAVs) [7], or visibility constraints [8].

Extensive research centered on quad-rotor unmanned aircraft vehicles (QUAVs) exhibits that IBVS algorithms have been formulated along with a handful of control strategies such as PID [9], sliding mode control (SMC) [10] [11] [12], adaptive sliding mode control (ASMC) [13], backstepping [14], model predictive control (MPC) [15], and fuzzy cognitive maps [16]. On one side, the PID controller struggles to stabilize the QUAV in a static test while being disturbed as in [17]. Meanwhile, the backstepping control handles disturbances in either dynamic movement or static tests with ease [18]. However, these estimated disturbances arise from the uncertainty of the model itself and the drag forces modeled by sinusoidal functions with a magnitude of 0.3 m/s^2. On the other hand, MPC delivers precision, but according to the author, it does not guarantee closed-loop stability for a cascaded controller, *i.e.* IBVS and MPC, as reported in [15]. Finally, sliding mode controllers prove to be more robust against bounded disturbances, with their adaptive variant providing the advantage of saving energy when compared to fixed-gain sliding mode techniques, as seen in [13], due to the non-overestimation of control gains. Furthermore, stability can be achieved using an IBVS-ASMC controller using the Lyapunov method as seen in [19]. Nevertheless, this adaptive variant has the disadvantage of increasing the complexity of the controller due to an increase in tuning parameters. Likewise, the magnitude of the gains may exhibit aggressive adaptations in some ASMC strategies which leads to system instability as concluded in [20]. Given these disadvantages, an ASMC that produces smoother gains and has reduced tuning parameters is desirable.

Therefore, the main contribution of this work is to develop an improvement of the aforementioned IBVS-ASMC controller by proposing a novel adaptive strategy: the single-gain adaptive sliding mode control (SGASMC). This strategy decreases the number of control parameters from four (μ, k, k_{min*}, K_2), as in [19] [21], to two (α, β). The SGASMC strategy is coupled with a non-singular fast terminal (NSFT) sliding surface to counter the highly disturbed environment a QUAV may encounter, ensure a finite-time convergence, eliminate non-singularities, and add a superior precision in contrast to other sliding surfaces even if the initial state has a large error [22] [23]. In consequence, hereon this combination will be denominated as an adaptive non-singular fast terminal (ANSFT) controller. Moreover, a Lyapunov stability analysis is provided for this improvement. Realistic disturbances are generated using the Von-Kármán wind turbulence model and added to the system as drag forces. Simulations demonstrate the capabilities and feasibility of the proposed ANSFT controller in a close to real-life situation.

The work is organized as follows: Section II presents QUAV modeling. Sections III and IV detail visual servoing design and its stability. Simulation results are addressed in section V. Lastly, conclusions are drawn.

II. QUAV Dynamics

This section introduces the Newton-Euler equations of motion for a standard quad-rotor UAV. Two reference frames are considered for the mathematical analysis. First, an inertial reference frame (X_I, Y_I, Z_I) with origin at a fixed point on Earth and a body reference frame (X_B, Y_B, Z_B) with origin at the center of mass of the rotorcraft, (see Fig. 1). Then, the

The authors are with Tecnológico de Monterrey, School of Sciences and Engineering, Monterrey, Nuevo León, México; a01196915@tec.mx; a00823922@tec.mx; a01421846@tec.mx; hermancc@tec.mx

linear and angular dynamics of the vehicle are stated as:

$$\dot{\boldsymbol{d}} = \boldsymbol{R}\boldsymbol{v} \tag{1}$$

$$m\dot{\boldsymbol{v}} = \boldsymbol{f} - m\boldsymbol{\omega} \times \boldsymbol{v} + \boldsymbol{R}^{-1}\boldsymbol{\delta} \tag{2}$$

$$\boldsymbol{f} = -T\boldsymbol{e_3} + \boldsymbol{R}^{-1}mg\boldsymbol{e_3} \tag{3}$$

$$\dot{\boldsymbol{\Theta}} = \boldsymbol{R_2}\boldsymbol{\omega} \tag{4}$$

$$\dot{\boldsymbol{\omega}} = \boldsymbol{J}^{-1}(\boldsymbol{\tau} - \boldsymbol{\omega} \times \boldsymbol{J}\boldsymbol{\omega}) \tag{5}$$

where vectors $\boldsymbol{d} = [x, y, z]^T$ and $\boldsymbol{\Theta} = [\phi, \theta, \psi]^T$ represent the inertial frame linear position and attitude, respectively. $\boldsymbol{v} = [u, v, w]^T$ and $\boldsymbol{\omega} = [p, q, r]^T$ stand for the body frame linear and angular velocities, respectively. Rotation matrix $\boldsymbol{R} \in \mathbb{R}^{3\times3}$ transforms data from the body frame to the inertial frame. Finally, $\boldsymbol{R_2} \in \mathbb{R}^{3\times3}$ (6), acts as a kinematic operator to map the angular accelerations, expressed by:

$$\boldsymbol{R_2} = \begin{bmatrix} 1 & s_\phi t_{g\theta} & c_\phi t_{g\theta} \\ 0 & c_\phi & -s_\phi \\ 0 & s_\phi/c_\theta & c_\phi/c_\theta \end{bmatrix} \tag{6}$$

Note that c_*, s_*, and t_{g*} stand for cosine, sine, and tangent functions. The linear forces acting on the aerial vehicle are enclosed in $\boldsymbol{f} = [f_x, f_y, f_z]^T$. $\boldsymbol{e_3} = [0, 0, 1]^T$ is a direction vector whereas m, g, and T represent the mass of the QUAV, gravity acceleration, and total thrust, respectively. The exerted torques vector is presented as $\boldsymbol{\tau} = [\tau_\phi, \tau_\theta, \tau_\psi]^T$. Moreover, assuming a symmetric quad-rotor vehicle, the moments of inertia matrix $\boldsymbol{J} \in \mathbb{R}^{3\times3}$ is given by diagonal matrix $\boldsymbol{J} = \text{diag}([J_{xx}, J_{yy}, J_{zz}])$. Finally, $\boldsymbol{\delta} = [\delta_x, \delta_y, \delta_z]^T$ stands for external disturbances as drag forces [24], expressed as:

$$\delta_\dagger = -\frac{1}{2}\rho c_\dagger \varepsilon_\dagger (\dot{d}_\dagger - v_{w\dagger})^2 \text{sign}(\dot{d}_\dagger - v_{w\dagger}) \tag{7}$$

where $\dagger = \{x, y, z\}$, ρ is the air density, c denotes the QUAV drag coefficient, whereas ε is the transversal area of the rotorcraft w.r.t each axis. The term $v_{w\dagger} \in \mathbb{R}$ defines the inertial frame wind velocity given by:

$$v_{w\dagger} = \bar{v}_{w\dagger} + \gamma_\dagger \tag{8}$$

Term $\bar{v}_{w\dagger} \in \mathbb{R}$ is the mean wind velocity and $\gamma_\dagger \in \mathbb{R}$ denotes wind deviations due to turbulent flow given by the Von Kármán wind model described in [25].

III. Image Features Extraction

In order to control the pose of a robot based on a visual reference, points of interest (POIs) are extracted from a downward camera installed at the center of mass of the QUAV. Then, a new camera reference frame $(X_C, Y_C, Z_C) \equiv (X_B, Y_B, Z_B)$ is introduced for the image data analysis. Moreover, a virtual camera approach is adopted to avoid possible singularities and local minima. This re-projection method is insensitive to roll and pitch rotations and involves the creation of a new virtual image plane and a virtual reference frame (X_ν, Y_ν, Z_ν) whose origin matches the body frame origin, as seen in Fig. 1. Consider a single POI p with inertial frame location $\boldsymbol{p}_I = [p_x, p_y, p_z]^T$. Then, its virtual frame position is given by:

$$\boldsymbol{p}_\nu = \boldsymbol{R}_\psi^T(\boldsymbol{p}_I - \boldsymbol{d}) \tag{9}$$

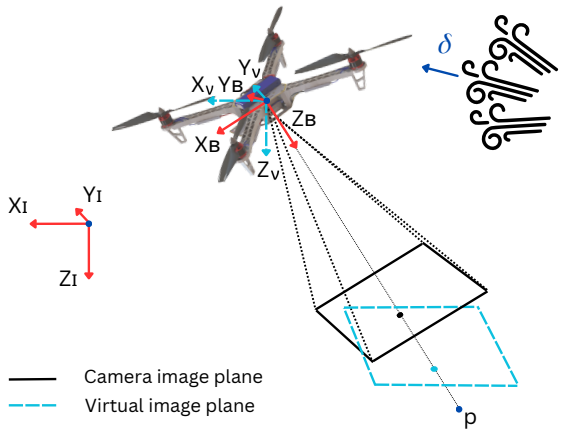

Fig. 1: QUAV model

with $\boldsymbol{R}_\psi \in \mathbb{R}^{3\times3}$ as the yaw rotation matrix. Furthermore, the time derivative of $\boldsymbol{p}_\nu$ is expressed as follows:

$$\dot{\boldsymbol{p}}_\nu = -\text{sk}(\dot{\psi}\boldsymbol{e}_3)p_\nu - \boldsymbol{v}_\nu + \boldsymbol{\kappa}_\nu \tag{10}$$

where $\text{sk}(\dot{\psi}\boldsymbol{e}_3) \in \mathbb{R}^{3\times3}$ represents a skew-symmetric matrix of vector $[0, 0, \dot{\psi}]^T$, $\boldsymbol{v}_\nu \in \mathbb{R}^3$ stands for the virtual frame linear velocity of the QUAV, and $\boldsymbol{\kappa}_\nu \in \mathbb{R}^3$ represents the virtual frame linear velocity of the target. Moreover, the projection of point p in the virtual image plane is computed by:

$$\begin{bmatrix} u_\nu & n_\nu \end{bmatrix} = f_0 \begin{bmatrix} \frac{p_{x_\nu}}{p_{z_\nu}} & \frac{p_{y_\nu}}{p_{z_\nu}} \end{bmatrix}^T \tag{11}$$

with pixel coordinates (u_ν, n_ν) and f_l as the focal length of the camera in meters units. In addition, the pixels from the camera image plane (u_c, n_c) can be transformed into the virtual image plane by employing the following expression:

$$\begin{bmatrix} u_\nu & n_\nu & f_l \end{bmatrix}^T = h\boldsymbol{R}_{\theta\phi} \begin{bmatrix} u_C & n_C & f_l \end{bmatrix}^T \tag{12}$$

where

$$h = \frac{f_l}{\boldsymbol{e}_3^T \boldsymbol{R}_{\theta\phi} \begin{bmatrix} u_C & n_C & f_l \end{bmatrix}} \tag{13}$$

and $\boldsymbol{R}_{\theta\phi} = \boldsymbol{R}_\theta \boldsymbol{R}_\phi \in \mathbb{R}^{3\times3}$. The image features to extract are based on the ordinary and centered image moments defined by $m_{ij_\nu} = \sum_{k=1}^N u_{k_\nu}^i n_{k_\nu}^j$ and $\mu_{ij_\nu} = \sum_{k=1}^N (u_{k_\nu} - u_g)^i (n_{k_\nu} - n_g)^j$ where N represents the number of POIs to track and i, j express the order of the moment. $u_g = \frac{m_{10_\nu}}{m_{00_\nu}}$ and $n_g = \frac{m_{01_\nu}}{m_{00_\nu}}$ are the coordinates from the centroid of the POIs. Adopting the strategy from [26], a feature normalization operation is applied to generate the linear image features vector $\boldsymbol{\zeta}_q \in \mathbb{R}^3$ with components:

$$\boldsymbol{\zeta}_q = \begin{bmatrix} \zeta_x & \zeta_y & \zeta_z \end{bmatrix}^T = \begin{bmatrix} \zeta_z \frac{u_{g_\nu}}{f_l} & \zeta_z \frac{n_{g_\nu}}{f_l} & \sqrt{\frac{\epsilon_d}{\epsilon}} \end{bmatrix}^T \tag{14}$$

with $\epsilon = \mu_{20_\nu} + \mu_{02_\nu}$ and ϵ_d as the reference value for ϵ. The dynamics of $\boldsymbol{\zeta}_q$ is given by:

$$\dot{\boldsymbol{\zeta}}_q = -\text{sk}(\dot{\psi}\boldsymbol{e}_3)\boldsymbol{\zeta}_q - \frac{1}{z_d}\boldsymbol{v}_\nu + \frac{1}{z_d}\boldsymbol{\kappa}_\nu \tag{15}$$

Additionally, take into account the term $\zeta_\psi \in \mathbb{R}$ as:

$$\zeta_\psi = \frac{1}{2}\arctan\left(\frac{2\mu_{11_\nu}}{\mu_{20_\nu} - \mu_{02_\nu}}\right) \tag{16}$$

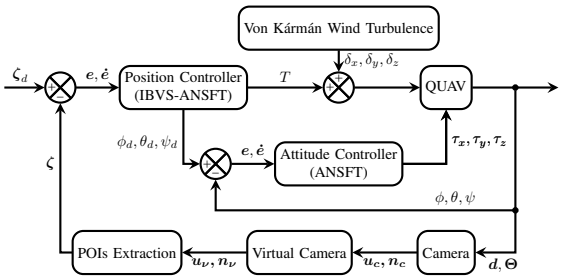

Fig. 2: IBVS-ANSFT control diagram.

with time-differentiation

$$\dot{\zeta}_\psi = \kappa_\psi - \dot{\psi} \tag{17}$$

The vector $\boldsymbol{\zeta}_q$ provides position measurements of the QUAV with respect to the target, while information regarding the relative heading of the rotor-craft is given by image feature ζ_ψ. Then, a new image features vector $\boldsymbol{\zeta} = [\zeta_x, \zeta_y, \zeta_z, \zeta_\psi]^T$ is introduced to provide positioning and heading feedback signals.

IV. IBVS-ANSFT Control design

This section details the design of an adaptive non-singular fast terminal image-based visual servoing for the positioning and heading control of a quad-rotor UAV. The aim is to provide enough robustness to the system such that the target to track remains inside the field of view of a downward camera even in the presence of bounded external disturbances. The control system consists of an outer-inner loop scheme where the IBVS-ANSFT strategy with reduced parameters is executed in the external loop while an internal loop attitude controller drives the fast dynamics of the vehicle, (see Fig. 2). Furthermore, the controller has been designed under the following assumptions:

Assumption 1. Initially the target is inside the field of view of the camera.

Assumption 2. The external disturbances vector $\boldsymbol{\delta}$ from (2) is bounded by $0 \leq ||\boldsymbol{\delta}|| \leq L_1$ with $L_1 > 0$.

Assumption 3. The full-state measurements from both QUAV and target are available. Additionally, the linear velocities and accelerations from the objective to track are bounded by $||\boldsymbol{\kappa}|| \leq Q_1$, and $||\dot{\boldsymbol{\kappa}}|| \leq Q_2$, respectively; with $Q_1, Q_2 \in \mathbb{R}^+$.

Assumption 4. The yaw rate and acceleration measurements from the target to track are bounded by $|\kappa_\psi| \leq Q_3$, and $|\dot{\kappa}_\psi| \leq Q_4$, respectively; with $Q_3, Q_4 \in \mathbb{R}^+$.

Consider the error signal vector

$$\boldsymbol{e} = \boldsymbol{\zeta_d} - \boldsymbol{\zeta} \tag{18}$$

where the reference $\boldsymbol{\zeta_d} = [0, 0, 1, 0]^T$ implies that the centroid of the target in the image matches the center of the complete virtual image plane. Then, by differentiation of $\boldsymbol{e}$; it results:

$$\dot{\boldsymbol{e}} = \begin{bmatrix} \frac{1}{z_d} & 0 & 0 & -\zeta_y \\ 0 & \frac{1}{z_d} & 0 & \zeta_x \\ 0 & 0 & \frac{1}{z_d} & 0 \\ 0 & 0 & 0 & 1 \end{bmatrix} \begin{bmatrix} v_{x_\nu} \\ v_{y_\nu} \\ v_{z_\nu} \\ \dot{\psi} \end{bmatrix} - \frac{1}{z_d} \begin{bmatrix} \kappa_{x_\nu} \\ \kappa_{y_\nu} \\ \kappa_{z_\nu} \\ z_d \kappa_\psi \end{bmatrix} \tag{19}$$

Then, without loss of generality, a non-singular fast terminal sliding surface is designed as:

$$\sigma_\star = e_\star + \lambda_{1,\star} |e_\star|^{\varphi_\star} \operatorname{sign}(e_\star) + \lambda_{2,\star} |\dot{e}_\star|^{\frac{\chi_\star}{\xi_\star}} \operatorname{sign}(\dot{e}_\star) \tag{20}$$

with $\star = \{x, y, z, \psi\}$, $\lambda_{1,\star}, \lambda_{2,\star} \in \mathbb{R}^+$, $1 < (\chi_\star / \xi_\star) < 2$, and $\varphi_\star > (\chi_\star / \xi_\star)$. Moreover, the time derivative of σ yields:

$$\dot{\sigma}_x = \Omega_{1,x} + \Omega_{2,x} \left[\frac{1}{z_d} \dot{v}_{x_\nu} - \zeta_y \ddot{\psi} - \dot{\zeta}_y \dot{\psi} - \frac{1}{z_d} \dot{\kappa}_{x_\nu} \right] \tag{21}$$

$$\dot{\sigma}_y = \Omega_{1,y} + \Omega_{2,y} \left[\frac{1}{z_d} \dot{v}_{y_\nu} + \dot{\zeta}_x \dot{\psi} + \zeta_x \ddot{\psi} - \frac{1}{z_d} \dot{\kappa}_{y_\nu} \right] \tag{22}$$

$$\dot{\sigma}_z = \Omega_{1,z} + \Omega_{2,z} \left[\frac{1}{z_d} \dot{v}_{z_\nu} - \frac{1}{z_d} \dot{\kappa}_{z_\nu} \right] \tag{23}$$

$$\dot{\sigma}_{\psi_\nu} = \Omega_{1,\psi} + \Omega_{2,\psi} \left[\ddot{\psi}_\nu - \frac{1}{z_d} \dot{\kappa}_{\psi_\nu} \right] \tag{24}$$

with terms $\Omega_{1,\star} = \dot{e}_\star + \lambda_{1,\star} \varphi_\star |e_\star|^{\varphi_\star - 1} \dot{e}_\star$ and $\Omega_{2,\star} = \lambda_{2,\star} \frac{\chi_\star}{\xi_\star} |\dot{e}_\star|^{\frac{\chi_\star}{\xi_\star} - 1}$. Then, the control law is derived as:

$$\begin{bmatrix} \dot{v}_{x_\nu} \\ \dot{v}_{y_\nu} \\ \dot{v}_{z_\nu} \\ \ddot{\psi}_\nu \end{bmatrix} = -z_d \begin{bmatrix} -\zeta_y \ddot{\psi} - \dot{\zeta}_y \dot{\psi} - \frac{1}{z_d} \dot{\kappa}_{x_\nu} + \iota_x - u_{a,x} \\ \dot{\zeta}_x \dot{\psi} + \zeta_x \ddot{\psi} - \frac{1}{z_d} \dot{\kappa}_{y_\nu} + \iota_y - u_{a,y} \\ -\frac{1}{z_d} \dot{\kappa}_{z_\nu} + \iota_z - u_{a,z} \\ \frac{1}{z_d} \left(-\frac{1}{z_d} \dot{\kappa}_{\psi_\nu} + \iota_\psi - u_{a,\psi} \right) \end{bmatrix} \tag{25}$$

with

$$\iota_\star = \frac{1}{\lambda_{2,\star} \frac{\chi_\star}{\xi_\star}} |\dot{e}_\star|^{2 - \frac{\chi_\star}{\xi_\star}} \operatorname{sign}(\dot{e}_\star) \left(1 + \lambda_{1,\star} \varphi_\star |e_\star|^{\varphi_\star - 1} \right) \tag{26}$$

and $u_{a,\star}$ as the SGASMC described by:

$$u_{a,\star} = -2 k_\star |\sigma_\star|^{\frac{1}{2}} \operatorname{sign}(\sigma_\star) - \frac{{k_\star}^2}{2} \sigma_\star \tag{27}$$

where $k_\star$ is the adaptive gain defined by adaptive law:

$$\dot{k}_\star = {\alpha_\star}^{\frac{1}{2}} |\sigma_\star|^{\frac{1}{2}} - {\beta_\star}^{\frac{1}{2}} {k_\star}^2 \tag{28}$$

where gains, $\alpha_\star, \beta_\star > 0$ stand for the precision and control effort parameters respectively. The non-singular fast terminal surface ensures a finite-time convergence, while the single-gain adaptive controller reduces the complexity of the system while providing robustness against bounded external disturbances and model uncertainties and avoiding the overestimation of its control gain. Notice that, in contrast to other adaptive methodologies, neither a minimal gain nor a sliding mode detector parameter is required for this scheme. This property improves the smoothness of the control signal, improving the behavior of the system. Now, by taking (2), the linear forces of the QUAV are expressed in the virtual reference frame as:

$$\boldsymbol{f}_\nu = m \mathrm{sk}(\dot{\psi} \mathbf{e_3}) \boldsymbol{v}_\nu + m \dot{\boldsymbol{v}}_{\boldsymbol{\nu}} \tag{29}$$

Then, the total motor thrust T is deduced as:

$$T = \boldsymbol{e_3}^T \boldsymbol{R_{\phi\theta}}(mg\boldsymbol{e_3} - \boldsymbol{f}_\nu) \tag{30}$$

where in simulation, the thrust is saturated to a maximum of 30 Newtons. In addition, the prior equation allows computing the desired roll and pitch rotations ϕ_d and θ_d as follows:

$$\phi_d = \arcsin(f_{y_\nu}/T) \tag{31}$$

$$\theta_d = \arcsin(-f_{x_\nu}/T\cos(\phi_d)) \tag{32}$$

Furthermore, the desired yaw rotation is given by:

$$\psi_d = \int\int \ddot{\psi}_\nu \, dt^2 \tag{33}$$

A. Attitude controller

The tracking of the desired rotations for the QUAV is performed by the proposed SGASMC controller. Thus, the sliding surface σ_* is designed as:

$$\sigma_* = e_* + \lambda_{1,*}|e_*|^{\varphi_*}\operatorname{sign}(e_*) + \lambda_{2,*}|\dot{e}_*|^{\frac{\chi_*}{\xi_*}}\operatorname{sign}(\dot{e}_*) \tag{34}$$

with $* = \{\phi, \theta, \psi\}$, and error signals $e_\phi = \phi_d - \phi$, $e_\theta = \theta_d - \theta$, and $e_\psi = \psi_d - \psi$. Then, the dynamics of σ_* are given by:

$$\dot{\sigma}_\phi = \Omega_{3,\phi} + \Omega_{4,\phi}\left[\ddot{\phi}_d - \frac{\tau_\phi}{J_{xx}} + \frac{J_{yy} - J_{zz}}{J_{xx}}\dot{\theta}\dot{\psi}\right] \tag{35}$$

$$\dot{\sigma}_\theta = \Omega_{3,\theta} + \Omega_{4,\theta}\left[\ddot{\theta}_d - \frac{\tau_\theta}{J_{yy}} + \frac{J_{zz} - J_{xx}}{J_{yy}}\dot{\phi}\dot{\psi}\right] \tag{36}$$

$$\dot{\sigma}_\psi = \Omega_{3,\psi} + \Omega_{4,\psi}\left[\ddot{\psi}_d - \frac{\tau_\psi}{J_{zz}} + \frac{J_{xx} - J_{yy}}{J_{zz}}\dot{\theta}\dot{\phi}\right] \tag{37}$$

with terms $\Omega_{3,*} = \dot{e}_* + \lambda_{1,*}\varphi_*|e_*|^{\varphi_*-1}\dot{e}_*$ and $\Omega_{4,*} = \lambda_{2,*}\frac{\chi_*}{\xi_*}|\dot{e}_*|^{\frac{\chi_*}{\xi_*}-1}$. Then, the control law for the attitude subsystem of the QUAV is expressed by:

$$\tau_\phi = J_{xx}\left[-\frac{J_{zz} - J_{xx}}{J_{yy}}\dot{\phi}\dot{\psi} - \ddot{\theta}_d + \eta_{\sigma,\theta} - u_{a,\theta}\right] \tag{38}$$

$$\tau_\theta = J_{yy}\left[-\frac{J_{yy} - J_{zz}}{J_{xx}}\dot{\theta}\dot{\psi} - \ddot{\theta}_d + \eta_{\sigma,\phi} - u_{a,\theta}\right] \tag{39}$$

$$\tau_\psi = J_{zz}\left[-\frac{J_{xx} - J_{yy}}{J_{zz}}\dot{\theta}\dot{\phi} - \ddot{\psi}_d + \eta_{\sigma,\psi} - u_{a,\psi}\right] \tag{40}$$

with $\eta_{\sigma,*}$ defined as:

$$\eta_{\sigma,*} = \frac{1}{\lambda_{2,*}\frac{\chi_*}{\xi_*}}|\dot{e}_*|^{2-\frac{\chi_*}{\xi_*}}\operatorname{sign}(\dot{e}_*)\left(1 + \lambda_{1,*}\varphi_*|e_*|^{\varphi_*-1}\right) \tag{41}$$

and $u_{a,*}$ is the SGASMC described in (27) and (28). Furthermore, torques for every rotation are saturated to 0.025 Newton-meter.

B. Stability analysis of the ANSFT

In this section, the stability of the proposed adaptive nonsingular fast terminal sliding mode controller with a single gain is addressed via Lyapunov theory. Bear in mind the following lemmas:

Lemma 3.1 [27]. Consider the nonlinear system and the sliding surface dynamics functions described by:

$$\begin{aligned}\dot{\zeta}_l &= f(x) + g(x)u_l \\ \dot{\sigma}_l &= f_\sigma(\zeta) + g_\sigma(\zeta)u_\sigma\end{aligned} \tag{42}$$

where u_σ is a sliding controller with an adaptive gain $k_l(t) \in \mathbb{R}^+$. Then, there is a positive constant k_l^+ such that

$$k_l(t) \leq k_l^+, \ \forall t > 0 \tag{43}$$

Lemma 3.2 [28]. Consider a system S defined as $\dot{\sigma} = G(\sigma)$ with G Lipschitz continuous and state $\sigma \in \mathbb{R}^n$. Given a valid continuous Lyapunov candidate function $V(\sigma) : \mathbb{R}^n \longmapsto \mathbb{R}^n$ where the next condition holds:

$$\dot{V}(\sigma) \leq -\eta V^\gamma(\sigma) + \varsigma, \qquad \eta \in \Re^{+*} \tag{44}$$

with $\eta \in \mathbb{R}^+$, $0 < \gamma < 1$, and $0 < \varsigma < \infty$. Then, practical finite-time convergence is achieved for $V(\sigma)$ at time t_c such that:

$$t_c \leq \frac{2V^{1-\gamma}(\sigma_0)}{\eta(1-\gamma)} \tag{45}$$

Theorem 3.1. *System considering the controller* (27) *with adaptive law* (28) *in closed loop with dynamics* (1)-(5) *expressed as:*

$$\dot{\sigma} = \Omega(-2k|\sigma|^{\frac{1}{2}}\operatorname{sign}(\sigma) - \frac{k^2}{2}\sigma + L_1) \tag{46}$$

where $\Omega = \lambda_2\frac{\chi}{\xi}|\dot{e}|^{\frac{\chi}{\xi}-1}$, *provides practical finite-time convergence of state* ζ, $\zeta \in \mathbb{R}$ *at a time* $t \leq t_c$.

Proof. Consider the following Lyapunov candidate function

$$V = \frac{1}{2}\sigma^2 + \frac{1}{2}(k - k^+)^2 \tag{47}$$

Following lemma 3.1, $k^+ \in \mathbb{R}^+$ is the upper-bound of adaptive gain k such that $(k - k^+) < 0$. Then the derivative of Lyapunov candidate function (47) yields:

$$\begin{aligned}
\dot{V} &= \sigma\dot{\sigma} + (k - k^+)\dot{k} && (48)\\
&\leq \Omega|\sigma|(-2k|\sigma|^{1/2} - \frac{k^2}{2}|\sigma| + L_1) \\
&\quad +(k - k^+)(\alpha^{1/2}|\sigma|^{1/2} - \beta^{1/2}k^2) && (49)\\
&\leq \Omega(-2k|\sigma|^{3/2} - \frac{k^2}{2}|\sigma|^2 + L_1|\sigma|) \\
&\quad +(k - k^+)(\alpha^{1/2}|\sigma|^{1/2} - \beta^{1/2}K^2) && (50)\\
&\leq \Omega(-2k(t)|\sigma|^{3/2} + 2k^+|\sigma|^{3/2} \\
&\quad -2k^+|\sigma|^{3/2} - \frac{k^2}{2}|\sigma|^2 + L_1|\sigma|) \\
&\quad +(k - k^+)(\alpha^{1/2}|\sigma|^{1/2} - \beta^{1/2}k(t)^2) && (51)\\
&\leq \Omega|\sigma|(-2k^+|\sigma|^{1/2} - \frac{k^2}{2}|\sigma| + L_1) && (52)\\
&\quad +(k - k^+)(\alpha^{1/2}|\sigma|^{1/2} - \beta^{1/2}k^2 - 2\Omega|\sigma|^{3/2})
\end{aligned}$$

Now introducing the parameters η_s and $\eta_k \geq 0$, where $\eta_s =$

$$2k^+|\sigma|^{1/2} + \tfrac{k^2}{2}|\sigma| - L_1$$

$$\begin{aligned}
\dot{V} &\leq \Omega|\sigma|\eta_s - \Omega|k-k^+|\eta_k + \Omega|k-k^+|\eta_k \qquad (53)\\
&\quad +(k-k^+)(\alpha^{1/2}|\sigma|^{1/2} - \beta^{1/2}k^2 - 2\Omega|\sigma|^{3/2})\\
&\leq \Omega|\sigma|\eta_s - \Omega|k-k^+|\eta_k \qquad (54)\\
&\quad +|k-k^+|(-\alpha^{1/2}|\sigma|^{1/2} + \beta^{1/2}k^2 + 2\Omega|\sigma|^{3/2} + \Omega\eta_k)\\
&\leq \Omega\left(\frac{\sqrt{2}|\sigma|}{\sqrt{2}}\eta_s - \frac{\sqrt{2}|k-k^+|}{\sqrt{2}}\eta_k\right) \qquad (55)\\
&\quad +|k-k^+|(-\alpha^{1/2}|\sigma|^{1/2} + \beta^{1/2}k^2 + 2\Omega|\sigma|^{3/2} + \Omega\eta_k)\\
&\leq -\Omega\min\{\sqrt{2}\eta_s, \sqrt{2}\eta_k\}\left(\frac{|\sigma|}{\sqrt{2}} + \frac{|k-k^+|}{\sqrt{2}}\right) \qquad (56)\\
&\quad +|k-k^+|(-\alpha^{1/2}|\sigma|^{1/2} + \beta^{1/2}k^2 + 2\Omega|\sigma|^{3/2} + \Omega\eta_k)
\end{aligned}$$

This can be rewritten to fit the form:

$$\dot{V} \leq -\eta V^{\gamma} + \varsigma, \qquad (57)$$

where $\eta = \Omega\min\{\sqrt{2}\eta_s, \sqrt{2}\eta_k\}$, $\gamma = 1/2$, $\varsigma = |k-k^+|(-\alpha^{1/2}|\sigma|^{1/2} + \beta^{1/2}k^2 + 2\Omega|\sigma|^{3/2} + \Omega\eta_k)$. Thus σ is practical finite-time stable if $\varsigma \in \mathbb{R}^+$. From the previous analysis, two cases arise:

- **Case 1.** If $|\sigma| = 0$, $\varsigma > 0$ if $\beta^{1/2}k^2 + \Omega\eta_k > 0$ due to the fact that β, k and Ω are defined positive then $\varsigma > 0\ \forall\eta_k > 0$. Therefore, finite time convergence is guaranteed once the system reaches the sliding surface.
- **Case 2.** If $|\sigma| \neq 0$, $\varsigma > 0$ if $-\alpha^{1/2}|\sigma|^{1/2} + \beta^{1/2}k^2 + 2\Omega|\sigma|^{3/2} + \Omega\eta_k > 0$ one can choose $\eta_k = (\alpha^{1/2}(\alpha^{1/2}/6\Omega)^{1/2})/\Omega$ to allow $\varsigma > 0$ during the reaching phase.

V. Simulation Results

In order to evaluate the proposed adaptive visual servoing strategy, a simulation was performed in a Gazebo/ROS environment. A video presenting this simulation is available on the following link: https://youtu.be/GprqokqhALo which was uploaded to the YouTube platform. The goal is that a QUAV is able to remain aligned with respect to a target even under wind perturbations. The target is a planar rectangular-shaped figure with an ArUco marker in each corner. The objective of the controller is to center the virtual image plane of the onboard QUAV camera against the centroid of the detected ArUco. The execution frequencies are 50 Hz for the outer loop and 100 Hz for both the inner loop of the controller and the QUAV dynamics. The target undergoes a perpetual linear and angular motion, its trajectory is defined by equations $x_t = 0.3\sin(0.1t)$, $y_t = 0.3\cos(0.1t)$, and $\psi_t = 0.1t$. To asses robustness, wind perturbations are applied at $20 \leq t \leq 60$ s, generated by the Von Kármán Wind Turbulence Model with parameters $\rho = 1.2$ Kg/m^3, $W_{20} = 15$ m/s, wingspan $w_s = 0.32$ m, and noise seeds $[23341, 23342, 23343, 23344]$. Mean wind velocities ($\bar{v}_{w\dagger}$) were defined as continuous sampled Gaussian noise signals whose parameters were frequencies of $f_x = f_y = f_z = 1$ Hz, standard deviations $\sigma_x = \sigma_y = \sigma_z = 1$ m/s, and means $\mu_x = \mu_y = 5$, and $\mu_z = 2$ m/s. The parameters for the ANSFT controller were set to $\lambda_{1_x} = \lambda_{1_y} = 4$, $\lambda_{1_z} = \lambda_{1_\psi} = 6$; $\lambda_{2_x} = \lambda_{2_y} = \lambda_{2_z} = \lambda_{2_\psi} = 3$; $\chi_x = \chi_y = \chi_z = \chi_\psi = 4$; $\xi_x = \xi_y = \xi_z = \xi_\psi = 3$; $\varphi_x = \varphi_y = 2.5$, $\varphi_z = \varphi_\psi = 2$ and $\alpha_x = \alpha_y = 0.008$, $\alpha_z = 0.5$, $\alpha_\psi = 0.05$; $\beta_x = \beta_y = \beta_z = 10$, $\beta_\psi = 5$. On the other hand, the angular ANSFT controller was designed with parameters $\lambda_{1_x} = 1$, $\lambda_{1_y} = \lambda_{1_y} = 0.5$; $\lambda_{2_x} = \lambda_{2_y} = \lambda_{2_z} = 1.2$; $\chi_x = \chi_y = \chi_z = 4$; $\xi_x = \xi_y = \xi_z = 3$; $\varphi_x = \varphi_y = \varphi_z = 1.8$ and $\alpha_x = \alpha_y = 10$, $\alpha_z = 1$; $\beta_x = 0.3$, $\beta_y = 0.1$, $\beta_z = 1$. Furthermore, the parameters of the drone were established as $\boldsymbol{d}(0) = [0.1, 0, -4]$ m, $\boldsymbol{\Theta}(0) = [0, 0, 0]$ rad, $m = 2$ Kg, $J_{xx} = 0.0411$ Kgm^2, $J_{yy} = 0.0478$ Kgm^2, $J_{zz} = 0.0599$ Kgm^2, $c_x = c_y = 0.3$, $c_z = 0.5$, $\varepsilon_x = \varepsilon_y = 0.1$ m^2 and $\varepsilon_z = 0.2$ m^2. Finally, the focal length of the camera has been established as $f_l = 0.00304$ m whereas the desired height with respect to the target was set to $z_d = 2.5$ m; implying that $\epsilon_d = 0.0000007970$. The complete trajectory executed by the QUAV in a 3D perspective is visualized in Fig. 4a. The rotorcraft reached the target and the desired altitude in a short time $t < 5$ s. The robustness provided by the adaptive controller allowed the aerial system to maintain its stability and the target inside the field of view of the camera despite the external disturbances and the oscillations due to drag forces. The POIs trajectories in the virtual image versus time are presented in Fig. 4b. Notice how in the beginning, the initial position of the target, denoted by circles, starts below the center of the image ($u < 0$) by a small amount. This is expected given that the QUAV started in front of the target by 0.1 m. Additionally, the resultant trajectories from the POIs demonstrate that the vehicle experienced heavy lateral wind gusts. On the other hand, the POIs are more separated from each other at their final positions, this is a visual demonstration of how if the QUAV descends, the POIs get separated from each other and as such, the control algorithm can calculate its height. Furthermore, Fig. 4c shows the position of the vehicle with respect to time. As expected, the real trajectory slightly deviates from the desired trajectory once the perturbations are present, but they never destabilize the system. The errors from the visual servoing are presented in Fig. 4d. It is clear that the yaw error behaves as a higher frequency signal in comparison to the other features, this is primarily due to the high variations in the attitude of the aircraft present in contrast to its *x*-*y*-*z* displacements. The adaptive control gains for the proposed IBVS-ANSFT scheme are illustrated in Fig. 4e. The gains increase once the simulation starts given that the QUAV is not perfectly aligned with its target. After the initial seconds, the adaptive parameters settle to the needed magnitudes for low control effort, then rise again to control the perturbations added to the system. Notice that, in comparison to the controller proposal in [19], the evolution of the IBVS gains was smoother throughout the disturbed scenario.

Now from the perspective of the attitude, the rotor-craft executed small roll and pitch rotations, as presented in Fig. 5b, despite the presence of wind perturbations. This constant attitude correction was needed throughout the whole simulation given the sinusoidal nature of the x and y trajec-

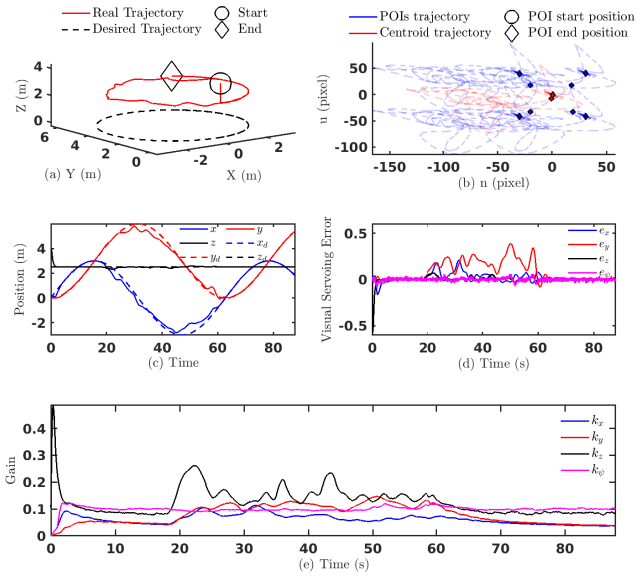

Fig. 4: QUAV simulation results. From left to right: (a) XYZ Positions (b) Virtual camera frame (c) Positions vs. time (d) Visual servoing errors (e) IBVS-Gains

tories executed by the target. Moreover, the aerial vehicle was capable of maintaining a satisfactory heading, giving a maximum yaw error of close to 0.05 rad, or 2.86 degrees (see Fig. 5d), when heavily perturbed. Referring to perturbations, consider the drag forces exerted on the vehicle in Fig. 3, these forces were derived from Eq. (7). Given the parameters of the random Gaussian signal that creates the mean wind velocities $(\bar{v}_{w\dagger})$, a maximum of approximately 30 km/hr gusts are to be expected. Considering the perturbations nature and the implementation of a virtual camera, some noise is to be expected within the exerted torques given in Fig. 5a, and the total thrust shown in Fig. 5c.

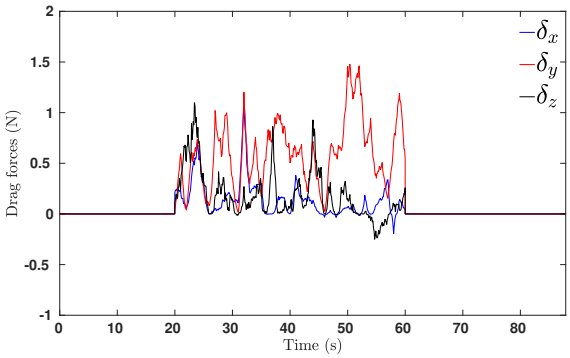

Fig. 3: Drag forces

Additionally, due to the quad-rotor being submitted to a perpetual angular motion, and the coupled dynamics of this system, minor corrections need to be applied during the test. This can be seen especially when the system experiences no perturbations at all.

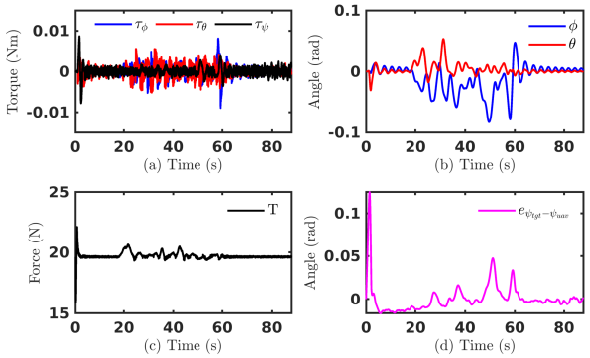

Fig. 5: SGASMC. From left to right: (a) Torques (b) Roll and pitch angles (c) Thrust (d) Yaw error target vs. QUAV

VI. Conclusion

A robust adaptive image-based visual servoing has been proposed for a quad-rotor unmanned aerial vehicle executing a target-tracking task in a perturbed scenario. Image features were acquired and processed to control the positioning and heading of the aerial vehicle. Moreover, a novel adaptive non-singular fast terminal sliding mode approach with minimal control parameters was implemented to handle the visual servoing error while reducing the complexity of the system and providing robustness against bounded external disturbances, smooth adaptive gain signals, and chattering attenuation. A Lyapunov stability analysis guaranteed the practical finite-time convergence of the closed-loop IBVS system. Finally, the proposal was evaluated through simulations using the Gazebo/ROS framework. The reported results demonstrated the sturdiness and effectiveness of the proposed strategy even in the presence of wind-turbulent fields of moderate intensity. Moreover, the next steps of this controller are to compare its performance against other well-known controllers and more importantly, to implement it on a real physical drone to observe the potential advantages and limitations of this proposed controller.

Acknowledgment

The researchers would like to thank the Multi-robot Systems Laboratory from Tecnologico de Monterrey for allowing the use of equipment and facilities for this research.

References

[1] F. Chaumette, S. Hutchinson, and P. Corke, "Visual servoing," *Springer handbook of robotics*, pp. 841–866, 2016.

[2] B. J. Nelson, J. D. Morrow, and P. K. Khosla, "Improved force control through visual servoing," in *Proceedings of 1995 American Control Conference-ACC'95*, vol. 1. IEEE, 1995, pp. 380–386.

[3] S. Hutchinson, G. D. Hager, and P. I. Corke, "A tutorial on visual servo control," *IEEE transactions on robotics and automation*, vol. 12, no. 5, pp. 651–670, 1996.

[4] C. Chen, S. Chen, G. Hu, B. Chen, P. Chen, and K. Su, "An auto-landing strategy based on pan-tilt based visual servoing for unmanned aerial vehicle in gnss-denied environments," *Aerospace Science and Technology*, vol. 116, p. 106891, 2021. [Online]. Available: https://www.sciencedirect.com/science/article/pii/S1270963821004016

[5] X. Sha, H. Sun, Y. Zhao, W. Li, and W. J. Li, "A review on microscopic visual servoing for micromanipulation systems: Applications in micromanufacturing, biological injection, and nanosensor assembly," *Micromachines*, vol. 10, no. 12, p. 843, 2019.

[6] R. Reyes and R. Murrieta-Cid, "An approach integrating planning and image-based visual servo control for road following and moving obstacles avoidance," *International Journal of Control*, vol. 93, no. 10, pp. 2442–2456, 2020.

[7] A. Keipour, G. A. Pereira, R. Bonatti, R. Garg, P. Rastogi, G. Dubey, and S. Scherer, "Visual servoing approach to autonomous uav landing on a moving vehicle," *Sensors*, vol. 22, no. 17, p. 6549, 2022.

[8] Y. Huang, M. Zhu, Z. Zheng, and K. H. Low, "Linear velocity-free visual servoing control for unmanned helicopter landing on a ship with visibility constraint," *IEEE Transactions on Systems, Man, and Cybernetics: Systems*, vol. 52, no. 5, pp. 2979–2993, 2021.

[9] X. Xiao, C. Wang, Y. Yang, Z. Li, and Z. Qin, "Autonomous tracking and landing of quav based on air-ground cooperation," in *2019 IEEE 28th International Symposium on Industrial Electronics (ISIE)*. IEEE, 2019, pp. 479–484.

[10] J. Chen, C. Hua, and X. Guan, "Image based fixed time visual servoing control for the quadrotor uav," *IET Control Theory & Applications*, vol. 13, no. 18, pp. 3117–3123, 2019.

[11] H. Bouzerzour, M. Guiatni, M. Hamerlain, and M. T. Boudali, "Robust uncooperative ground target surveillance using vision-based sliding mode control of quadrotor uav," in *IECON 2022 – 48th Annual Conference of the IEEE Industrial Electronics Society*, 2022, pp. 1–8.

[12] H. Bouzerzour, M. Guiatni, A. Allam, Y. Bouzid, and M. Hamrelain, "Robust vision-based sliding mode control for uncooperative ground target searching and tracking by quadrotor," *Unmanned Systems*, 2023.

[13] A. Miranda-Moya, H. Castañeda, J. Gordillo, and H. Wang, "Ibvs based on adaptive sliding mode control for a quadrotor target tracking under perturbations," *Mechatronics*, vol. 88, p. 102909, 2022.

[14] W. He and L. Yuan, "Image-based finite-time visual servoing of a quadrotor for tracking a moving target," *Nonlinear Dynamics*, vol. 111, no. 6, pp. 5307–5328, 2023.

[15] P. Roque, "Coordination of multi-agent systems: Predictive and vision-based control for aerial and space robotics," Ph.D. dissertation, KTH Royal Institute of Technology, 2022.

[16] A. Amirkhani, M. Shirzadeh, E. I. Papageorgiou, and M. R. Mosavi, "Fuzzy cognitive map for visual servoing of flying robot," in *2016 IEEE international conference on fuzzy systems (FUZZ-IEEE)*. IEEE, 2016, pp. 1371–1376.

[17] M. Cheong, M. Bahiki, and S. Azrad, "Development of collision avoidance system for useful uav applications using image sensors with laser transmitter," in *IOP Conference Series: Materials Science and Engineering*, vol. 152, no. 1. IOP Publishing, 2016, p. 012026.

[18] W. He and L. Yuan, "Global finite-time control for image-based visual servoing of quadrotor using backstepping method," *Journal of Vibration and Control*, p. 10775463221108542, 2022.

[19] A. Miranda-Moya, H. Castañeda, and H. Wang, "Image-based visual servoing via nonsingular fast terminal adaptive sliding mode control for a quadrotor uav subjected to wind fields," in *2022 IEEE 61st Conference on Decision and Control (CDC)*. IEEE, 2022, pp. 3104–3109.

[20] D. K. Villa, A. S. Brandão, and M. Sarcinelli-Filho, "Adaptive sliding mode control applied to quadrotors-a practical comparative study," *Journal of the Franklin Institute*, 2023.

[21] A. Miranda-Moya, H. Castañeda, and H. Wang, "Turbulent wind gusts estimation and compensation via high-gain extended observer-based adaptive sliding mode for a quadrotor uav," in *2021 International Conference on Unmanned Aircraft Systems (ICUAS)*. IEEE, 2021, pp. 476–481.

[22] S. Venkataraman and S. Gulati, "Control of nonlinear systems using terminal sliding modes," 1993.

[23] L. Yang and J. Yang, "Nonsingular fast terminal sliding-mode control for nonlinear dynamical systems," *International Journal of Robust and Nonlinear Control*, vol. 21, no. 16, pp. 1865–1879, 2011.

[24] A. Aboudonia, R. Rashad, and A. El-Badawy, "Composite hierarchical anti-disturbance control of a quadrotor uav in the presence of matched and mismatched disturbances," *Journal of Intelligent & Robotic Systems*, vol. 90, pp. 201–216, 2018.

[25] S. Gage, "Creating a unified graphical wind turbulence model from multiple specifications," in *AIAA Modeling and simulation technologies conference and exhibit*, 2003, p. 5529.

[26] O. Tahri and F. Chaumette, "Point-based and region-based image moments for visual servoing of planar objects," *IEEE Transactions on Robotics*, vol. 21, no. 6, pp. 1116–1127, 2005.

[27] F. Plestan, Y. Shtessel, V. Bregeault, and A. Poznyak, "New methodologies for adaptive sliding mode control," *International journal of control*, vol. 83, no. 9, pp. 1907–1919, 2010.

[28] Y. Shtessel, C. Edwards, L. Fridman, and A. Levante, *Sliding Mode Control and Observation*. Springer, 01 2014, pp. 291–320.